

Accurate Determination of the Mass Distribution in Spiral Galaxies:

3. Fabry-Perot Imaging Spectroscopy of 6 Spiral Galaxies

S. Blais-Ouellette^{1,2,3}, P. Amram², C. Carignan³, and R. Swaters^{4*}

¹ Department of Astronomy, California Institute of Technologies, CA 91125, USA

² Laboratoire d'Astrophysique de Marseille, 2 Place Le Verrier, F-13248 Marseille Cedex 04, France

³ Département de physique and Observatoire du mont Mégantic, Université de Montréal, C.P. 6128, Succ. centre ville, Montréal, Québec, Canada. H3C 3J7

⁴ Carnegie Institution of Washington, Washington DC 20015, USA

Received / Accepted

Abstract. An abstract should be given

1. Introduction

Λ CDM N-body numerical simulations, predict that the innermost parts of density profiles are cuspy: e.g. Navarro et al. (1996) predict an inner slope $\alpha = -1.0$ while Moore et al. (1999) finds an inner slope $\alpha = -1.5$. On the other hand, the observational results do not confirm these cosmological predictions but strongly suggest that dark halos have a constant central density (inner slope closer to $\alpha = 0$ than to $\alpha = -1$; e.g. de Blok et al., 2003; Swaters et al., 2003; Blais-Ouellette et al., 1999, 2001). Despite the observational evidences that the central density profiles of dark matter halos are better represented by a flat core than by a cusp, Navarro et al. (2003), using high resolution N-body simulations (down to 0.5 per cent of r_{200}), continue to defend that the fitting formula proposed by NFW provides a reasonably good approximation to the density and circular velocity profiles of individual halos. Furthermore, they introduce a new fitting formula with a steeper slope to alleviate some of the differences with Moore et al. (1999). This seems at odds with observations, especially of dwarf and LSB galaxies.

This is the third paper in a series on high resolution Fabry-Perot spectroscopy of spiral galaxies. The first paper (Blais-Ouellette et al., 1999, hereafter paper I) showed the necessity of optical integral field spectroscopy to accurately determine the rotation curves in the inner parts of spiral and dwarf galaxies. The main reason being that

HI rotation curves are affected by beam smearing, a natural consequence of their low spatial resolution (Begeman, 1987; Swaters, 1999b; van den Bosch et al., 2000). In combination with paper II (Blais-Ouellette et al., 2001), paper I also brought to light the great sensitivity of the mass distribution parameters to the inner rotation curve. The ideal rotation curve is therefore a combination of high resolution optical integral field spectroscopy and sensitive HI radio observations extending well beyond the luminous disk (see also Sofue et al., 1999, for high resolution CO data). Paper II has also shown the difficulties in reconciling dwarf and late type galaxies rotation curves with standard CDM N-body simulations (e.g. Navarro et al., 1996, 1997; Moore et al., 1998, 1999). While those simulations do not have the resolution to make definite predictions at small radii, an extrapolation of the functional form derived at larger radii predicts cuspy density profiles, implying much steeper inner slopes than observed in these galaxies. Rotation curves of all galaxy types were also shown to be more compatible with flat core density profiles.

The first step in showing the reality of this discrepancy is to eliminate the known possibilities of systematic observational biases. Two classes of error can contribute to the underestimation of the velocities, hence of the computed halo density, in the inner parts of spiral galaxies. The prime culprit in radio observations is the “beam smearing” effect due to the relatively low angular resolution of 21 cm data. Typically the radio beam is too large to resolve the inner disk velocity gradient. Combining the HI density gradient with the true velocity gradient inside

Send offprint requests to: S. Blais-Ouellette

* SBO, PA and CC, Visiting Astronomers, Canada-France-Hawaii Telescope, operated by the National Research Council of Canada, the Centre National de la Recherche Scientifique de France, and the University of Hawaii.

Table 1. Parameters of the sample. Columns 4,5,6,10 and 11 are from the main reference unless otherwise specified.

Name	Type	Dist. Mpc	D_{25} ''	R_{HO} ''	α^{-1} ''	i^{p3} °	PA^{p3} °	V_{sys}^{p3} km s^{-1}	M_B	L_B $10^8 L_\odot$	Ref.
UGC 2259	SBcd	9.6*	2.6	1.9	28.2	41	165	581	-17.03	9.7	C88
NGC 2403	SABcd	3.2 ^{Fr}	21.9	13.0	134	61	126	137	-19.50	93.6	C90
NGC 6946	SABcd	6.2 ^{Sh}	11.5	7.8	115.2	38	60	47	-21.38	530	Be
NGC 5055	SABc	9.2*	12.6	9.8	108.9	64	101	501	-21.13	422	Th
NGC 2841	SAB	14.1 ^{Ma}	11.3	6.2	52	66	150	633	-21.93	880	Be
NGC 5985	SABb	33.5*	5.5	2.7	29.9	58	15	2515	-21.74	738	p3

^{p3}This studyCol 4: Diameter at the 25 B-mag/arcsec² isophote^{Be}Begeman (1987)

Col 5: Holmberg radius

^{C88}Carignan et al. (1988)

Col 6: Scale length

^{C90}Carignan et al. (1990)

Col 7: Inclination

^{Fr}Freedman (1990)

Col 8: Position angle of the major axis

^{Ma}Macri et al. (2001)

Col 9: Systemic heliocentric velocity

^{Sh}Sharina et al. (1997)

Col 10: Absolute B magnitude

ThThornley and Mundy (1997)

Col 11: Total B luminosity

* $H_0 = 75 \text{ km s}^{-1} / \text{Mpc}$

a beam width will most likely lead to underestimate the velocity at a given radius.

$H\alpha$ observations always easily reach an angular resolution where any spatial resolution effect can be neglected. A less often commented source of uncertainties though is found in long slit observations, where most of the $H\alpha$ data come from. Schommer et al. (1993) was the first large scale publication of rotation curves derived from Fabry-Perot data. They clearly state the inherent advantages of 2D spectroscopy over long slit observations. Beauvais and Bothun (1999, 2001) were among the first to do Fabry-Perot imaging spectroscopy of nearby, large angular size late type spirals for the express purpose of performing precision mass modeling. They detailed the advantages that 2D velocity fields have over 1D slits. Beauvais and Bothun (2001) discussed precision quality rotation curves and optimal rotation curve fitting. One can point to the lack of 2D coverage that makes the alignment of the slit crucial to retrieve the real kinematics of a galaxy. First, a photometrically determined inclination can be a major source of uncertainty. Second, missing the kinematical center, which is not always the photometric center (paper II) can lead to an underestimation of the rotational velocities. Also, just a degree or two between the slit and the galaxy position angle for highly inclined galaxies can cause the highest velocity regions along the line of nodes to be missed. This in turn leads to underestimate the rotational velocities. In a series of papers started in 1992 (referenced in Amram et al., 1996), a large sample of rotation curves of nearby galaxies in clusters, derived from Fabry-Perot, have also shown the observational biases avoided when using 3D data cubes instead of long slits data. In addition, the presence of a bar would hardly be noticed in long slit data and its effect would most probably be confounded with the rotational kinematics, while 2D velocity fields allow to disentangle circular from radial motions.

This paper extends our sample of multi-wavelength velocity fields to earlier morphological types by adding

six spiral galaxies to the optical rotation curves sample with available 21 cm data. Contrary to dark matter dominated dwarf spirals and to luminous matter dominated early type spirals, the stellar disk and dark halo of intermediate type have comparable contributions to the mass inside the Holmberg radius. Therefore, a slight change of the inner slope of the rotation curve can significantly reduce or increase the disk contribution, whether it is maximal or best-fitted. This change can induce a dramatic difference in the dark matter distribution by increasing or limiting its inner density, as seen in the case of NGC 5585 in Blais-Ouellette et al. (1999). The halo core radius and central density are indeed very sensitive to the exact baryonic contribution at low radii. This is true for halos of all shapes, but more critical for cuspy halos, which often have problem to accommodate for the presence of even a small disk in later type spirals (Blais-Ouellette et al., 2001).

Section 2 briefly describes the sample while section 3 explains the Fabry–Perot observations and data reduction, and presents the main features of each galaxy. Computed $H\alpha$ velocity fields and rotation curves are also described therein, and compared to HI rotation curves. Dynamical analysis and mass models will be given in a forthcoming paper (paper IV). Section 4 presents a discussion of the main results and the main conclusions.

2. The sample

Table 1 summarizes the optical parameters of each galaxy in the sample. Neutral hydrogen kinematics and mass models of UGC 2259 and NGC 6946 have been studied by Carignan et al. (1988, 1990) while NGC 2403 and NGC 2841 are part of Begeman’s thesis (1987). All these studies present rotation curves based on 21 cm observations from the Westerbork Synthesis Radio Telescope (WSRT). NGC 5985 is part of the Westerbork HI survey of spiral

and irregular galaxies^a (WHISP, see Swaters et al., 2000). An HI rotation curve derived from these data is presented in this paper, but the details on the HI observations for this galaxy will be published elsewhere. An HI rotation curve of NGC 5055, based on VLA observations, has been published by Thornley and Mundy (1997).

This sample expands the range of morphological types from the very late types of paper II to earlier (Sc to Sb) types. The GHASP survey^b Garrido et al. (2002), an ongoing Fabry-Perot survey will expand this sample to about 200 spiral galaxies.

3. Fabry–Perot observations: data acquisition and reduction

All the Fabry-Perot observations have been initially made at the Canada–France–Hawaii Telescope (CFHT) in September 97 and March 98 using the CFHT1 high resolution Fabry-Perot etalon installed in the Multi-Object Spectrograph (MOS) focal reducer. A narrow-band filter ($\Delta\lambda \simeq 12 \text{ \AA}$), centered around the systemic velocity of the observed object, was placed in front of the etalon. The available field with negligible vignetting was $\approx 8.5' \times 8.5'$, with $0.44'' \text{ pix}^{-1}$. The free spectral range of 5.66 \AA (258 km s^{-1}) was scanned in 27 (+1 overlapping) channels for UGC 2259, NGC 6946 and the blue side of NGC 5055 (see section 3.4), giving a sampling of 0.21 \AA (9.6 km s^{-1}) per channel. For the rest of the sample, the objects were scanned in 24 channels, for a sampling of 0.24 \AA (10.8 km s^{-1}). Due to the use of an aging filter which has apparently blueshifted from its quoted central wavelength, the fluxes from the receding half of NGC 2841 and NGC 5055 were almost totally blocked, and these galaxies had to be re-observed. The details are given in the relevant sections.

Following normal de-biasing and flat-fielding with standard IRAF procedures, a robust 3-D cosmic-ray removal routine, that tracks cosmic rays by spatial (pixel-to-pixel) and spectral (frame-to-frame) analysis, was applied to every data cube. When necessary, ghost reflections were then removed using the technique described in Paper I. A neon line ($\lambda_{6598.95} \text{ \AA}$) was used for absolute wavelength calibration at each pixel.

The signal measured along the scanning sequence was split into two parts: (1) an almost constant level produced by the continuum light in a narrow passband around $H\alpha$ (hereafter referred to as continuum map) and (2) a varying part produced by the $H\alpha$ line (hereafter referred to as $H\alpha$ emission line map *or* monochromatic map). The continuum level was taken to be the mean of the channel which do not contain the line. The $H\alpha$ integrated flux map was obtained by integrating the monochromatic profile in each pixel above the threshold defined by the continuum level. The scanning of the interferometer sufficiently samples the PSF of the instrument (the Airy function con-

Table 2. Parameters of the Fabry–Perot observations.

Date of observations	September 97, March 98
Telescope	3.6 m CFHT ^a
Instrumentation:	
Instrument	MOSFP
CCD detector	2048×2048 , $\sigma = 8 e^{-1}$
Filters:	
UGC 2259:	$\lambda_0 = 6575 \text{ \AA}$, $\Delta\lambda = 13 \text{ \AA}$
NGC 2403:	$\lambda_0 = 6568 \text{ \AA}$, $\Delta\lambda = 12 \text{ \AA}$
NGC 6946:	$\lambda_0 = 6566 \text{ \AA}$, $\Delta\lambda = 12 \text{ \AA}$
NGC 5055 blue:	$\lambda_0 = 6575 \text{ \AA}$, $\Delta\lambda = 13 \text{ \AA}$
red:	$\lambda_0 = 6586 \text{ \AA}$, $\Delta\lambda = 12 \text{ \AA}$
NGC 2841 blue:	$\lambda_0 = 6577 \text{ \AA}$, $\Delta\lambda = 10 \text{ \AA}$
red:	$\lambda_0 = 6587 \text{ \AA}$, $\Delta\lambda = 11 \text{ \AA}$
NGC 5985:	$\lambda_0 = 6621 \text{ \AA}$, $\Delta\lambda = 26 \text{ \AA}$
Fabry–Perot unit	Scanning QW1162 (CFHT1)
Calibration lamp	Neon ($\lambda = 6598.95 \text{ \AA}$)
Interference order	1155 @ λ_{NEON}
Mean Finesse	12
Duration:	
UGC 2259:	8 min/channel (3.6 h)
NGC 2403:	7.34 min/channel (2.9 h)
NGC 6946:	7.5 min/channel (3.4 h)
NGC 5055 blue:	9.42 min/channel (3.8 h)
red:	6 min /channel (2.7 h)
NGC 2841 ^a :	5 min/channel (2 h)
NGC 5985:	7.7 min/channel (3.1 h)
Spatial Parameters	
Field size	$8.5' \times 8.5'$
Pixel scale	$0.44'' \text{ pix}^{-1}$
Spectral parameters	
Free spectral range at $H\alpha$	5.66 \AA (258 km s^{-1})
NGC 2403, 5055, 5985:	
Number of channels	24
Sampling	0.24 \AA (10.8 km s^{-1})/channel
UGC 2259 and NGC 6946:	
Number of channels	27
Sampling	0.21 \AA (9.6 km s^{-1})/channel
NGC 2841 ^a :	
Free spectral range at $H\alpha$	8.30 \AA (378 km s^{-1})
Number of channels	24
Sampling	0.35 \AA (15.8 km s^{-1})/channel

^a NGC 2841 was reobserved at the Observatoire de Haute Provence. See text.

volved by the surface and transmission defects) and covers the free spectral range through 24 to 27 scanning steps. When the profiles are structureless and the S/N high, the lines could be successfully fitted by the convolution of the observed PSF (given by the narrow Neon-6598.95nm emission line) and a single Gaussian function. When the profile is more complex, multiple Gaussian components are needed. Nevertheless, since the number of scanning steps and the baseline of the continuum emission are relatively low, and the structure of the profile is often complex (asymmetries, multiple components, low S/N), we do not fit a function to the profile to extract the first order momentum. Instead, the heliocentric radial velocity for a given pixel is directly given by the position of the

^a www.astro.rug.nl/~whisp

^b <http://www-obs.cnrs-mrs.fr/interferometrie/ghasp.html>

barycentre of the line. Furthermore, we do not have to make assumptions on the fit used when the data are dominated by Poisson’ or receptor’ noise at low S/N levels. However, at high S/N, since we have a good knowledge of the PSF, the barycentre of the emission line profile may be measured with an accuracy much better than the sampling step, hence giving a precision of about 3 km/s for a S/N=5. For each pixel, the S/N level is given by the y-axis of the barycentre of the line normalized by the r.m.s of the continuum. When the S/N of each individual pixel was not high enough to derive a radial velocity, two different Gaussian smoothings were performed on the cubes ($\sigma = 2.6''$ and $4''$) in order to get sufficient signal-to-noise throughout the images. Three velocity maps (one for each smoothed cube and for the original) were then obtained from the intensity weighted means of the H α peaks at each pixel. A final variable resolution velocity map was constructed keeping higher resolution where the signal-to-noise makes it possible. Figs. 1 and 3 show the monochromatic images of the galaxies while Figs. 2 and 4 display their velocity fields^c. Table 2 lists the main observing parameters.

Rotation curves were derived using two different methods: velocity dispersion minimization (tilted-ring model: Begeman, 1987; Côté et al., 1991) and rotation curve symmetry optimization by comparing the approaching and receding sides. The first method is more precise and allow to model a warp disk, while the second is more robust and is useful for galaxies with low S/N and patchy velocity coverage. In all cases all the parameters (systemic velocity, kinematical center, inclination, and position angle) were initially free to vary.

To date, no convention on the way to represent the errors on rotation curves exists in the literature. Error bars are often simply given as the velocity dispersion in the ring used at each radius. However, the warm gas tends to be found in more disturbed environments than the cold gas. Turbulence, local density variations (like spiral arms) and winds from stars and supernovae of the young stellar forming regions in which the gas is ionized, increase its dispersion. This can lead to the paradox where fewer points (as in long-slit observations) lead to lower dispersion and to smaller error bars. As a more direct probe of the uncertainties on the measured potential, the difference between the two sides of the galaxy is instead sometimes used. Some authors add the error due to uncertainties on inclination and/or position angles.

Since the purpose of this study is to present the data in an unbiased way, the sources of errors are given separately. The error bar itself gives the error on the mean in each ring (σ/\sqrt{N}) while the solutions for each side of the galaxy are represented by continuous lines for the receding side and dashed lines for the approaching. Errors due to inclination uncertainties are given by $V(\sin i + \epsilon - \sin i - \epsilon)$ where ϵ is around 2 for all the galaxies. Other parameters (Table 1)

have low uncertainties and contribute marginally to the velocity error budget.

3.1. UGC 2259

This small galaxy was observed in September 97 by a fairly photometric night. Eight minutes integration were spent at each channel position and no photometric corrections were needed.

Like in the case of IC 2574 (paper II), dispersion minimizing methods as in ROCUR are hardly applicable to determine the rotation curve because of the incomplete coverage of the velocity field. The rotation curve was thus found by comparison of the two sides of the galaxy and analysis of the residual velocity field using the ADHOC package^d. The inclination, position angle and systemic velocity were fixed at 41° , 158° and 581 km s^{-1} , in fairly good agreement with Carignan et al. (1988). The H α coverage of the field is patchy and mainly concentrated in the center and in the two spiral arms. The net effect is to have only the receding side covering the innermost part of the rotation curve. However, because the two sides cover the outer parts and agree fairly well, this lack of coverage should only affect the determination of the kinematical center, adding some uncertainty to the rotation curve. The resulting optical rotation curve at $2.6''$ resolution is given in Table A.1 while Fig. 5 presents it in combination with the HI rotation curve.

As one can see in Fig.2, only a few clumps of ionized gas reveal the very inner kinematics of the galaxy. The solid body rise can now be observed within a few hundreds of parsecs on the receding side. The H α curve is higher than the HI by 5 to 10 km s^{-1} up to a radius of $50''$. Even if this is an indication of the presence of beam smearing in the uncorrected HI observations, we cannot exclude non-circular motions due to the lack of coverage.

The most prominent feature of the H α rotation curve is the big dip around $60''$. This is not observed in the HI curve. It can be seen in the velocity field that the location of this feature corresponds to the two great spiral arms, clearly identified in the optical image (see e.g. Carignan et al., 1988). Spiral arms are known to create such effect, especially on the ionized gas (e.g. Thornley and Mundy, 1997).

Fabry-Perot observations of UGC 2259 by Gonzalez-Serrano and Valentijn (1991) using the brightest HII regions and the new data are consistent within the error bars.

In conclusion, even if the kinematical parameters derived for UGC 2259 reach a reasonable level of confidence, the asymmetric distribution of H α emission and the relatively low covering factor weaken this galaxy contribution as a test case.

^c All the velocity maps are available at www.astro.caltech.edu/~sbo/vf.html

^d <http://www.oamp.fr/adhoc/adhoc.html>

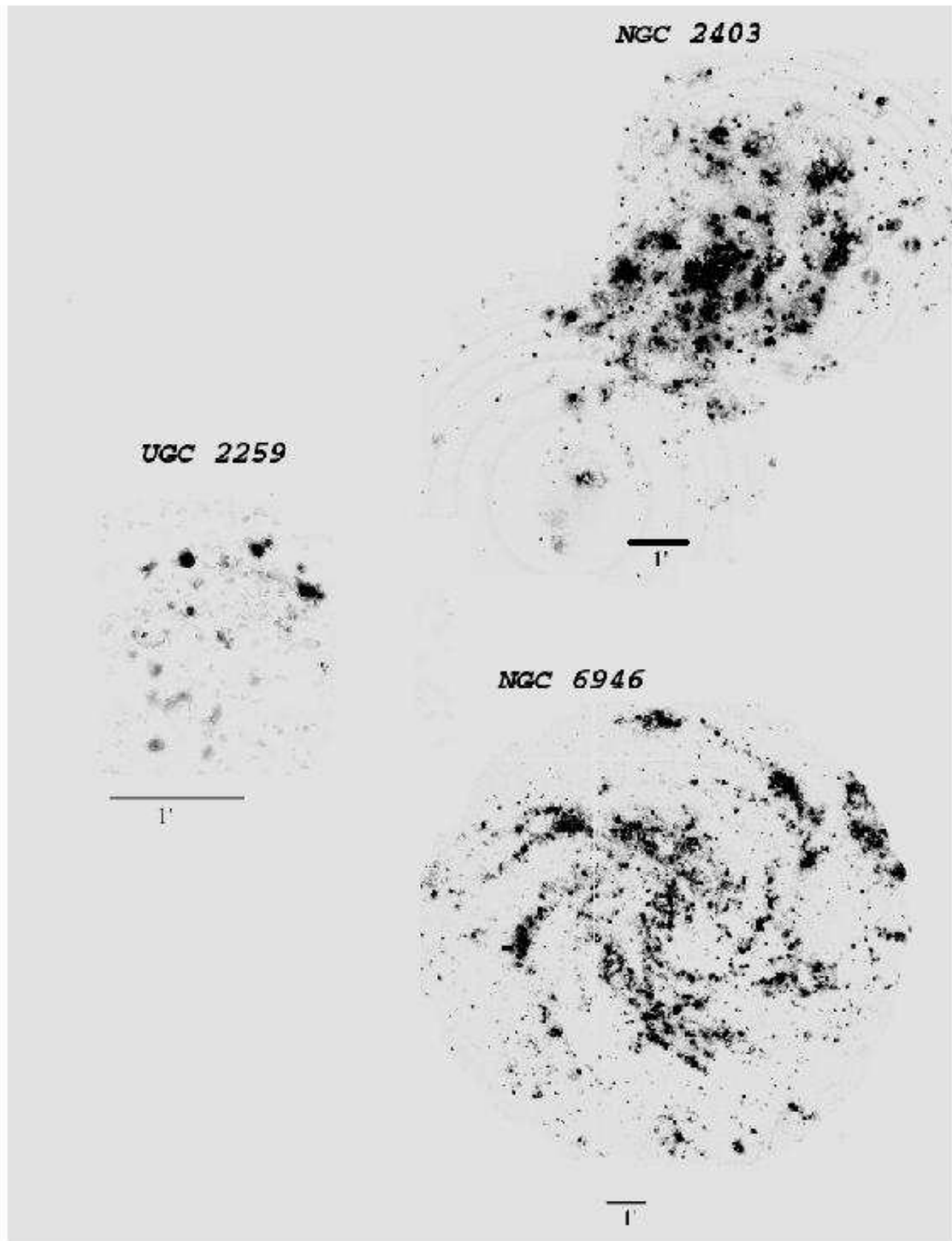


Fig. 1. Monochromatic images of the H α flux of UGC 2259, NGC 2403 and NGC 6946. North is up, East is left.

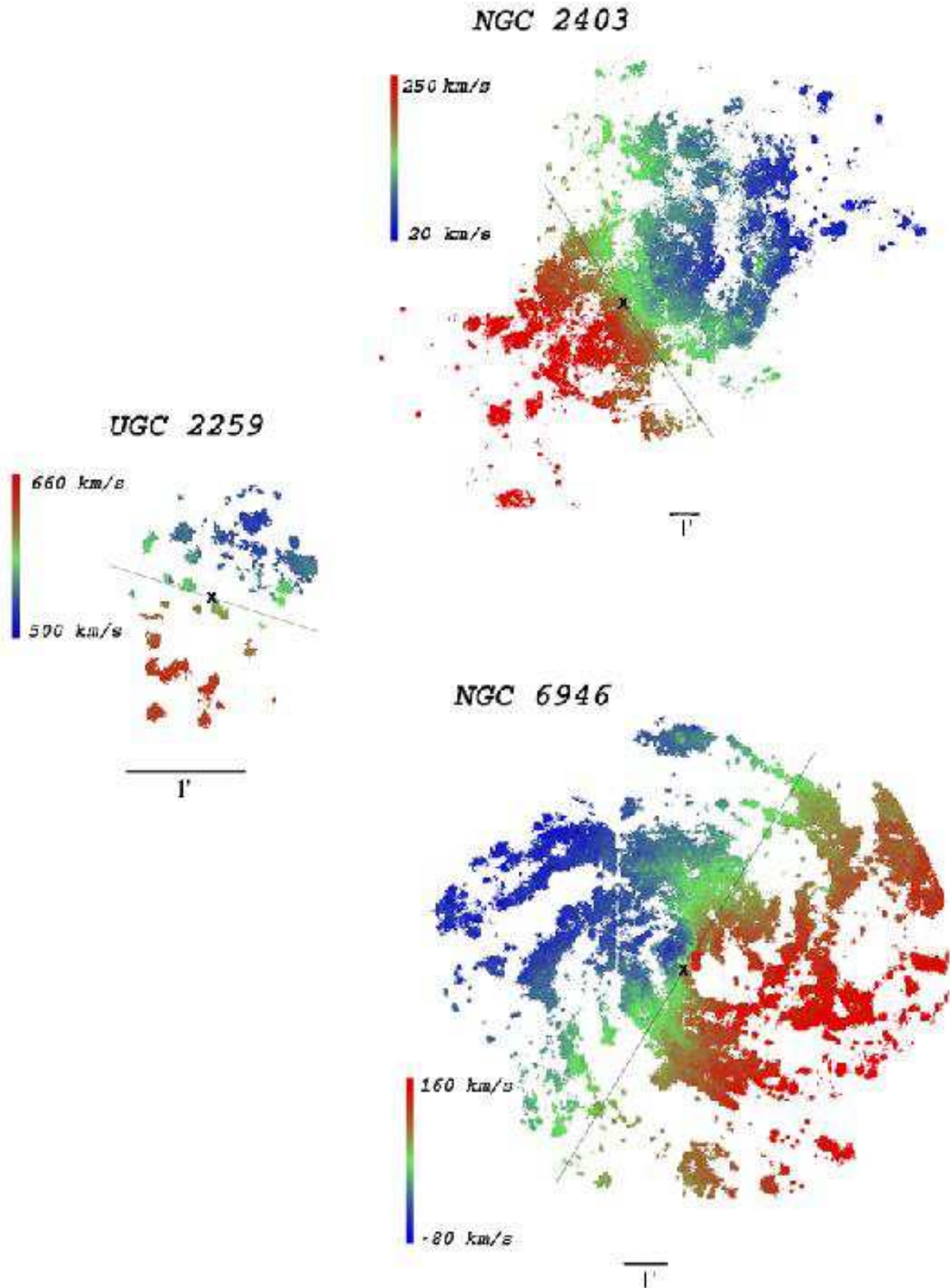


Fig. 2. Velocity fields of the same galaxies. The X and the grey line indicate the kinematic center and the axis of rotation, respectively, for each galaxy.

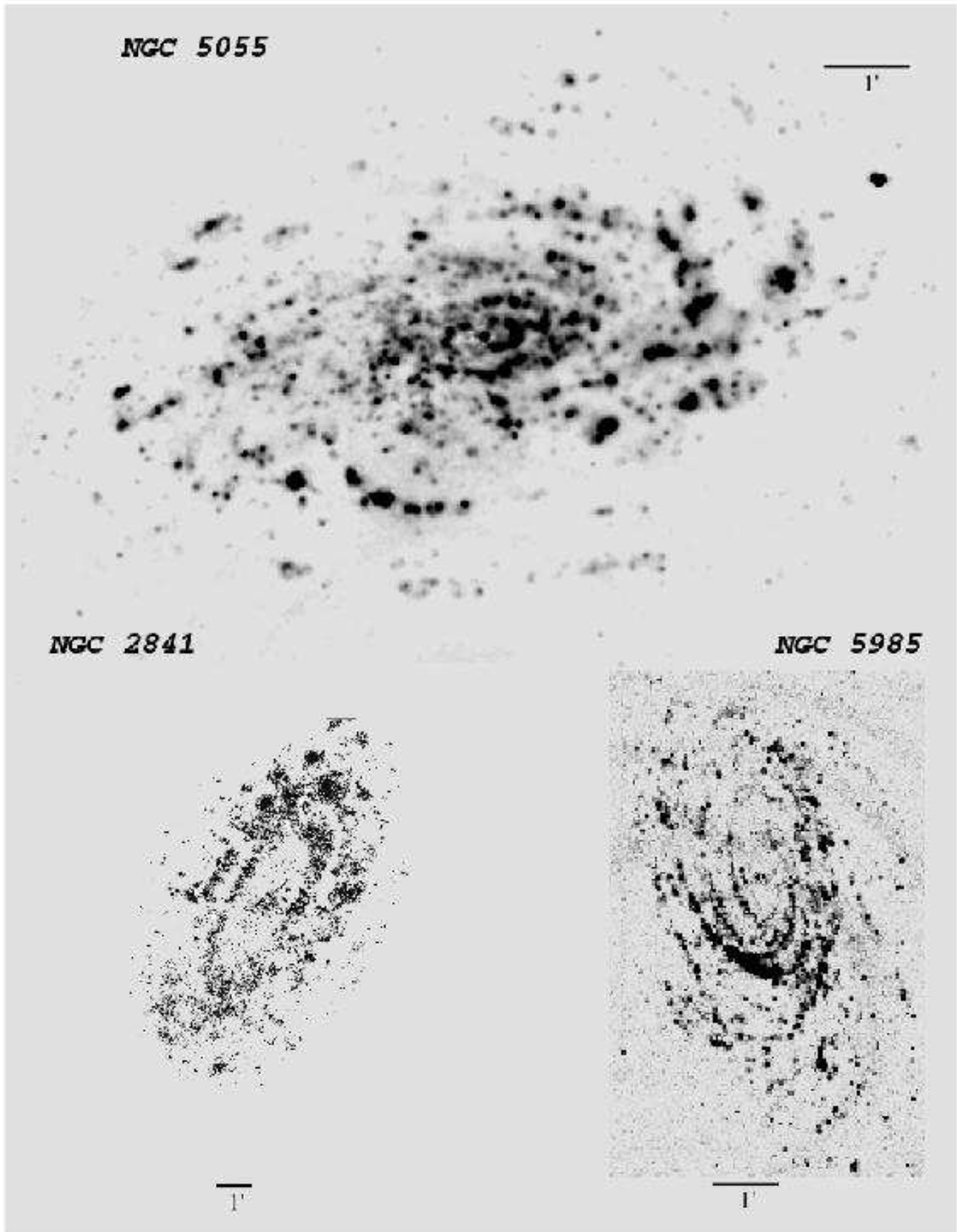


Fig. 3. Monochromatic images of the $H\alpha$ flux of NGC 5055, NGC 2841 and NGC 5985

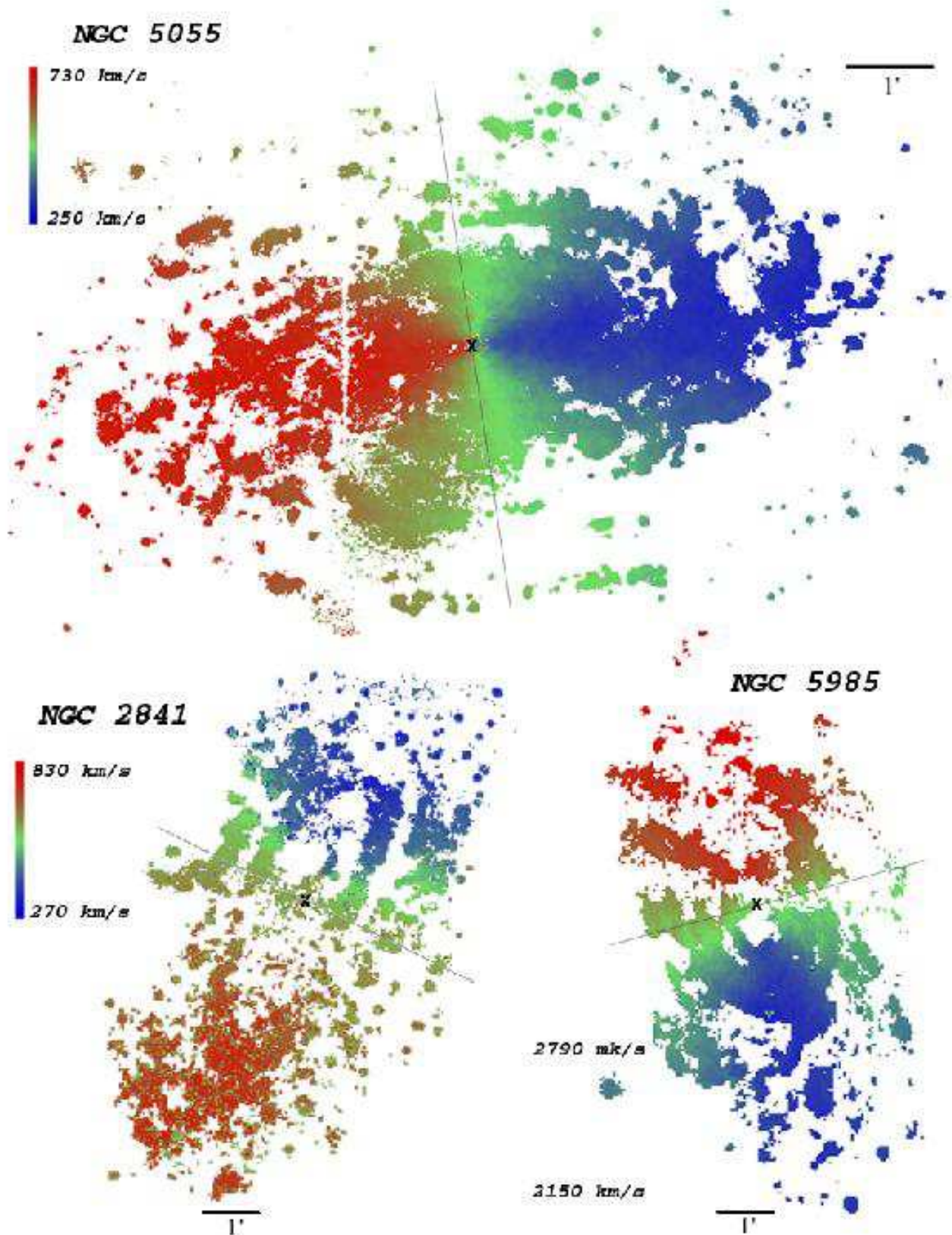


Fig. 4. Velocity fields of the same galaxies.

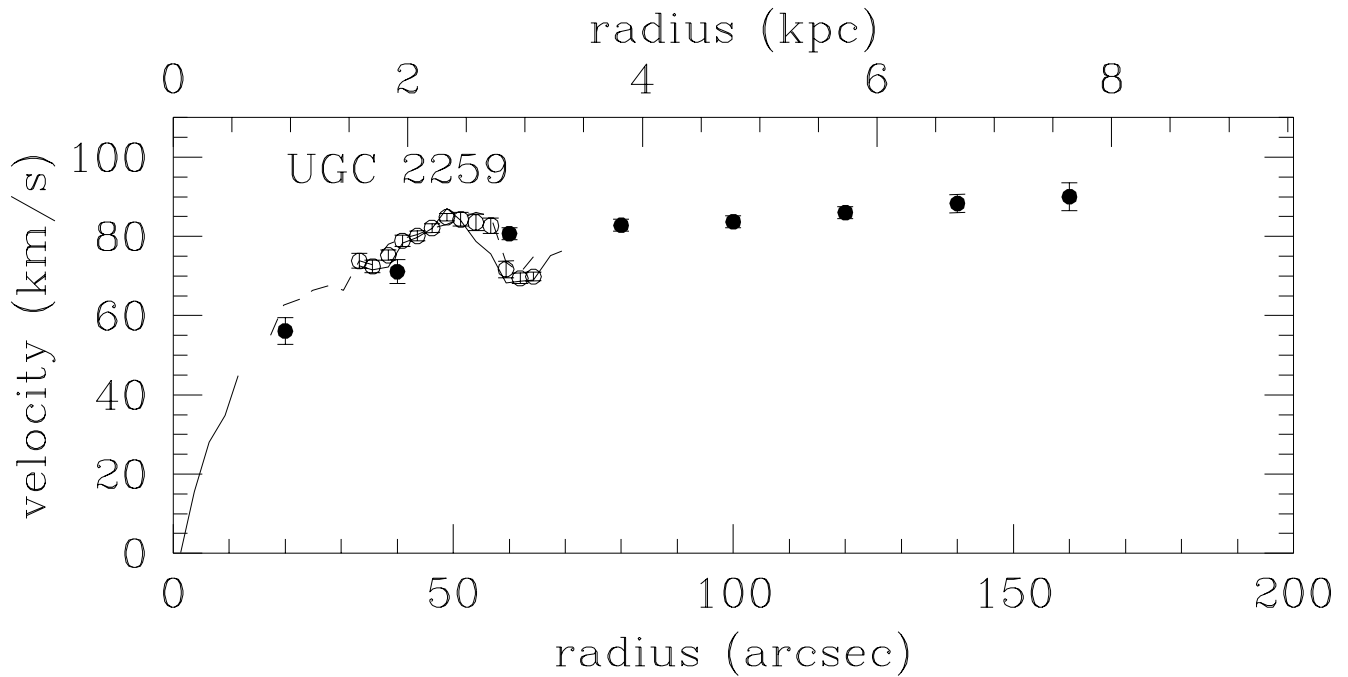


Fig. 5. $H\alpha$ rotation curve of UGC 2259 (open circles). Approaching and receding sides from $H\alpha$ data are indicated respectively by the dashed and continuous lines. The filled circles represent the HI rotation curve from Carignan et al. (1988).

3.2. NGC 2403

The object being larger than the available field, two data cubes were acquired during the run of March 98. The same parameters were used for both fields and 440 seconds were spent on each of the 24 channels of each data cube. After the standard data reduction, the final maps (velocity, continuum and monochromatic) were joined using stars in the overlapping region. The coverage of the field was this time complete enough to use ROCUR with bins of 20 arcsec. However, since no significant variations of inclination or position angle were found, ADHOC was used to get a higher sampling. The inclination was found to be 61° , the position angle 126° and the systemic velocity 137 km s^{-1} , at 3 km s^{-1} of Begeman's value. The shape of the rotation curve is independent of the resolution used and bins of 5 pixels ($6.6''$) offer the clearest picture. Fig. 6 shows the final rotation curve. The HI curve is also plotted for comparison. The Fabry-Perot data show a remarkable agreement between the approaching and receding sides up to $200''$. At a greater radius, the number of points on the receding side drops sharply (see Table A.2) and the curve then relies mainly on the approaching side.

The inner limit of the big external arm is located around $200''$ and the effect of the arm can clearly be seen on both sides of the rotation curve. The full resolution velocity map gives an even clearer picture as it shows the effect of the arm at different galactic longitudes. The south-eastern arm is less obvious on the monochromatic image and seems dominated by a few giant HII regions. This explains the bumpy appearance of the receding curve

above $200''$ where each HII region produces a bump and increase the dispersion. Only the approaching side is seen above $470''$ and relies only on a few HII regions.

3.3. NGC 6946

The central part of this bright Scd galaxy suffers from a lack of $H\alpha$ emission. Despite the 3.5 hours of observation that otherwise gave the sensitivity to reach down to the smaller HII region and the diffuse ionized gas, few $H\alpha$ photons were collected up to $50''$ in radius. The velocity dispersion is high in that region and makes the true kinematics hard to retrieve. This appears clearly in the rotation curve presented in Fig. 7 and in Table A.3.

Between $70''$ and $100''$, the rotation curves on both sides are smooth but present a big asymmetry, indicative of non circular motions, most probably gas movement along a central bar (Bonnarel et al., 1988). The presence of dust (Roussel et al., 2001) explains the lack of $H\alpha$ emission and is compatible with a mild starburst occurring at the center. This starburst is likely to play a role in the high velocities observed near the center, considering that the relatively low mass of the molecular gas, a few percent of the stellar mass (Israel and Baas, 2001), could not explain such high rotational velocities in the inner part.

The rest of the rotation curve (resolution of $4.4''$) matches the HI curve. The systemic velocity is found to be 47 km s^{-1} in agreement with Carignan et al. (1990) but not consistent with the 38 km s^{-1} found by Bonnarel et al.

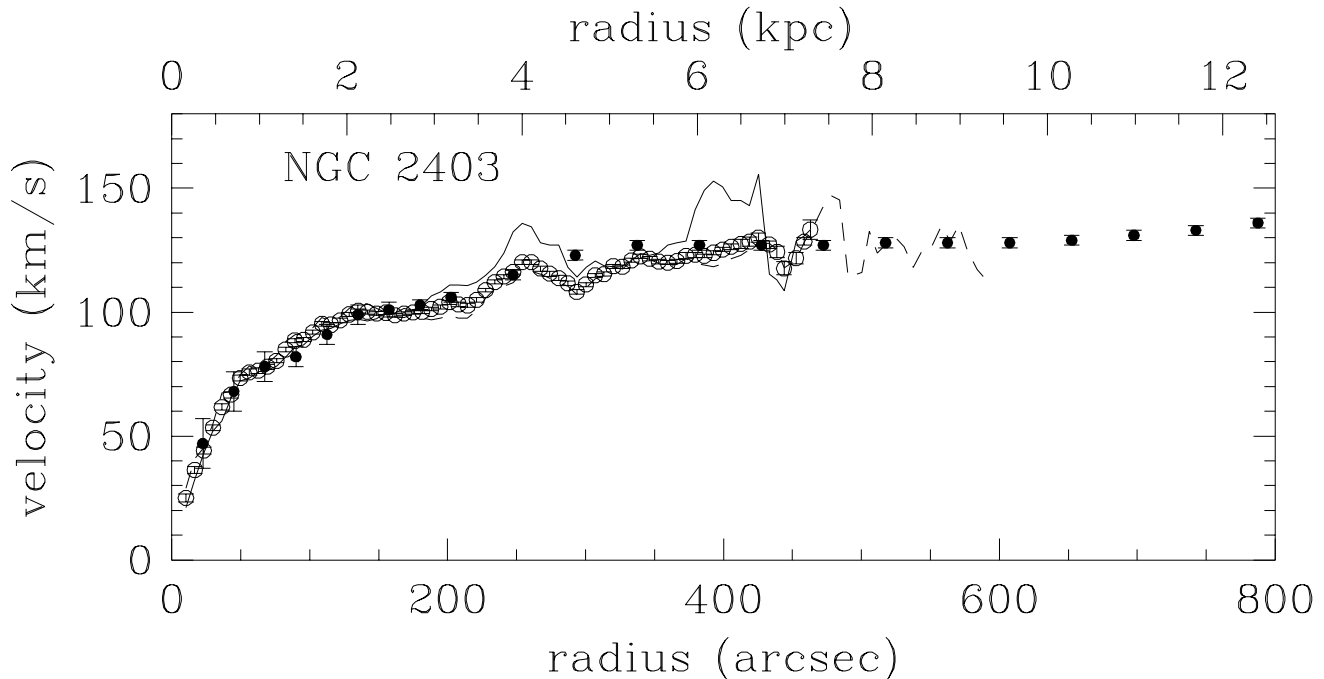


Fig. 6. $H\alpha$ rotation curve of NGC 2403 (open circles). Approaching and receding sides from $H\alpha$ data are indicated respectively by the dashed and continuous lines. The filled circles represent the HI rotation curve from Begeman (1987).

(1988). However, the inclination and position angles are less constrained due to the uncertainties caused by the global asymmetry. They are compatible with both Bonnarel ($i = 32^\circ$ and $PA = 58^\circ$) and Carignan et al. ($i = 38^\circ$ and $PA = 60^\circ$). They were fixed to the latter for ease of comparison. It has to be noted that the uncertainty on the inclination can affect the velocities dramatically (as $\sin i$). For example, Sofue (1996) uses an optically determined inclination of 30° in conjunction with his CO data along the major axis and ends up with velocities 20% higher. That recalls the importance of having a complete 2-D coverage to allow an independent determination of optical parameters.

3.4. NGC 5055

This object was first observed in March 98 but the interference filter used had blueshifted as explained in section 3. To complete the data set, it has been observed again in April 99 using a redder filter. Both sets of data were analyzed following the standard procedure and two full resolution data cube were produced. They have then been combined using field stars and their spectral zero point matched with high accuracy in overlapping regions.

For the majority of bright galaxies where the kinematics have been investigated in detail, the optical and dynamical centers do coincide (Begeman, 1987). For some late-type barred galaxies the shifts between both center determinations could be larger than 1 kpc (e.g. de Vaucouleurs and Freeman, 1972;

Beauvais and Bothun, 2001; Weldrake et al., 2003). For low surface brightness galaxies, due to their faintness, the determination of the morphological center could in itself be a problem, nevertheless de Blok et al. (2003) conclude that the offsets between optical and dynamical centers are small. We have tested for NGC 5055 the influence of a “kinematic sloshing of the center of mass” on the spatial scale of 500 pc and we conclude that whether inclination and position angles were kept fixed at the value derived by Thornley and Mundy (1997) or let free to vary (in which case the averages are 64° and 99°), the $H\alpha$ rotation curve (Fig. 8 and A.4) ranges systematically from 2 to 11 km s^{-1} above the HI curve. This fact is hard to understand especially in view of the otherwise general good agreement between the two curves. Pismis et al. (1995) published a long-slit based rotation curve that tends to be slightly lower than the present Fabry-Perot curve. However, because of its limit in radius ($70''$), it is hardly reliable to solve the discrepancy. In an early paper, van der Kruit and Bosma (1978) derived an optical rotation curve from the inner 60 arcsec regions of NGC 5055. Taking into account the difference of inclination the agreement with our rotation curve is reasonable.

Two important differences exist between the HI and $H\alpha$ curves. First, the central $H\alpha$ points are up to 30 km s^{-1} higher than their HI counterparts. Second, it can be noticed that the amplitude of the velocity variations due to the passage of the spiral arms (at radii around 60'' and 120'') are much more pronounced in the $H\alpha$ data than in HI. The velocity difference can be in part nat-

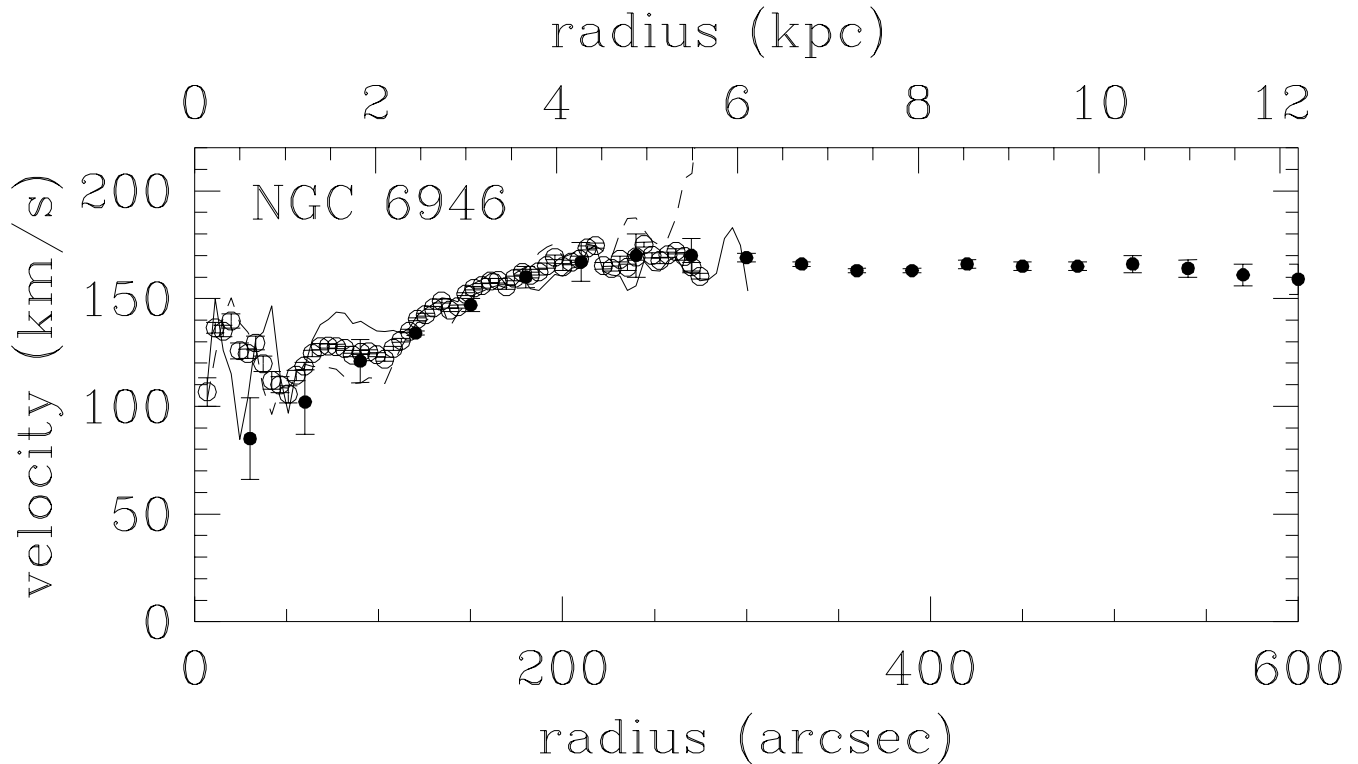


Fig. 7. $H\alpha$ rotation curve of NGC 6946 (open circles). Approaching and receding sides from $H\alpha$ data are indicated respectively by the dashed and continuous lines. The filled circles represent the HI rotation curve from Carignan et al. (1990)

urally associated with beam smearing in the 21 cm observations. However, its amplitude, the strength of the response to arm, and especially the difference between approaching and receding sides show an important component of streaming motion, in agreement with the finding of Thornley and Mundy (1997). Averaging velocities from both sides helps removing the effect of this non-circular motion and retrieving the equivalent rotational kinematics. Nonetheless, this galaxy is a good illustration of the ionized gas sensitivity to its environment, due to the short time scale of kinematic feedback from star formation processes.

The ~ 8 arcsec region around the center of this galaxy is very peculiar and will be termed "the central region". At the adopted distance of 9.2 Mpc, the linear extension is ± 360 pc. This dense central region is roughly 6 times brighter in the continuum than the nearby surrounding region and about 25 times in the $H\alpha$ line. An important fraction of the pixels of this central region shows two emission lines. When separated in two velocity components (fig. 9) two drastically different velocity patterns appear. One pattern shows slightly disturbed kinematics, but still consistent with the global disk kinematics. The second component shows two regions of high peculiar velocities compatible with an almost counter-rotating disk or with a bipolar outflow. In case of a disk, its position angle is 220° , 121° from the galaxy major axis. The disk inclination can hardly be retrieved due to the small region

with clear nuclear emission line. Peculiar spectral features seem to affect a region extending to around $18''$, but they are mostly buried in the main disk component. Because of this extent, inclination is most probably lower than 70° , and $V\sin i \simeq 111 \text{ km s}^{-1}$ up to 300 pc. The systemic velocity is 10 km s^{-1} lower than the galaxy systemic velocity, a difference similar to the velocity error bars. These velocities lead to a $M\sin i \simeq 9 \pm 2 \times 10^8 M_\odot$ inside 300 pc.

However, the quasi constant velocities throughout this component, and the much brighter blue side, are more consistent with a bipolar outflow. Pismis et al. (1995) already interpreted a departure from pure rotation on the blue side as such. Their long slit data did not allow the detection of the red component, but they probably detected the bright blue clump north-east of the center. However, Afanasiev and Sil'chenko (2002) note that a south-west anomaly (our red clump) is also present in their stellar velocities, a rather puzzling fact if the outflow interpretation is retained.

3.5. NGC 2841

First observed at CFHT with the same blueshifted filter as NGC 5055, this galaxy was reobserved in December 2001 at the Observatoire de Haute-Provence (France) in the context of the GHASP survey. The instrumentation used at the OHP is very similar to the one used at the CFHT with the exception that the detector was a photon count-

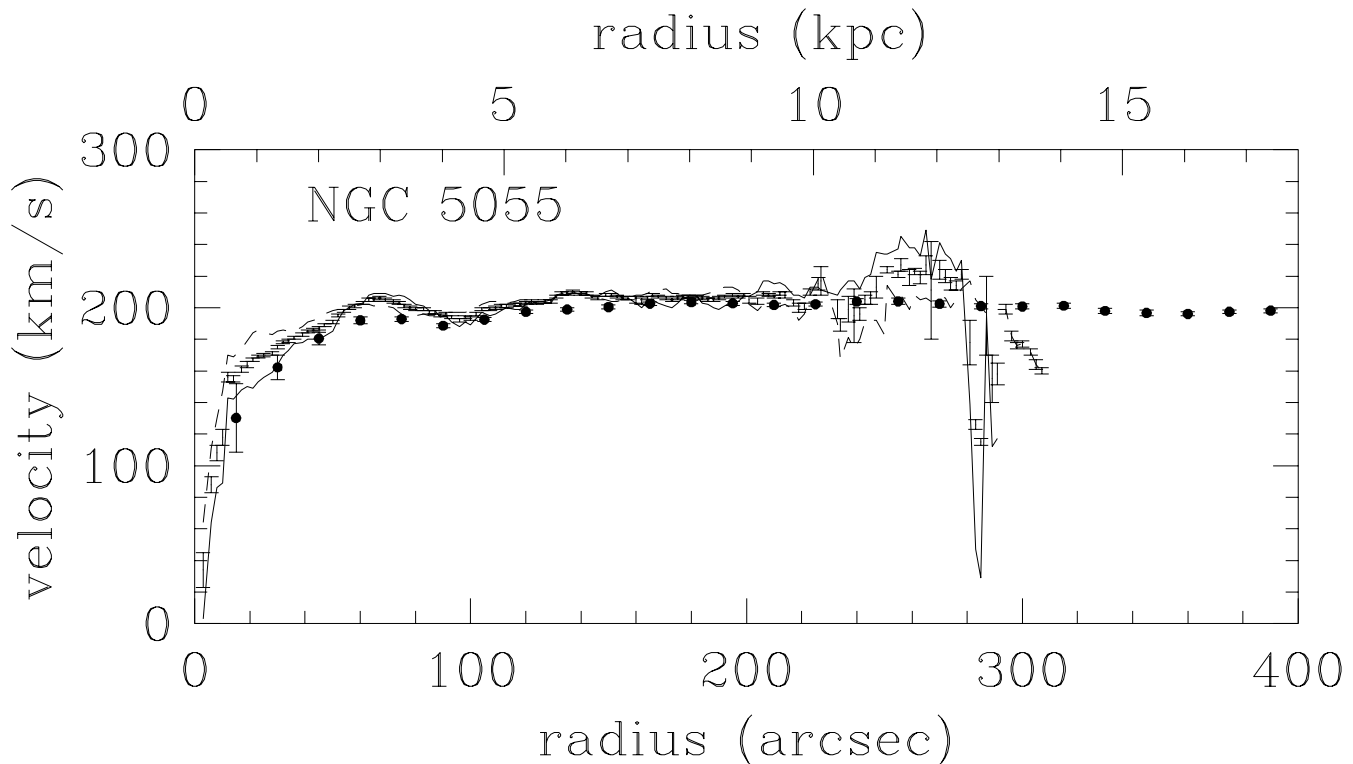


Fig. 8. $H\alpha$ rotation curve of NGC 5055 (error bars alone). Approaching and receding sides from $H\alpha$ data are indicated respectively by the dashed and continuous lines. The filled circles represent the HI rotation curve from Thornley and Mundy (1997).

ing system instead of a CCD. Because photon counting cameras have intrinsically no read-out noise, it is possible to rapidly scan through the 24 channels several times, averaging photometric variations of the sky. It is then easier to remove night sky emission lines and background light (Amram et al., 1995). The filter used at the OHP was matched to the receding side of the galaxy. Joining the two velocity fields using stars in the field, a complete coverage was achieved. Despite filters well matched to the galaxy velocities, we confirm the overall low $H\alpha$ luminosity already noted by Kennicutt (1988). NGC 2841 is one of the coldest galaxies in the entire IRAS survey having a 60/100 ratio as low as M31, another galaxy greatly deficient in H-alpha. Data from 2MASS show normal effective colors with $J-H = 0.71$ and $H-K = 0.23$ implying a normal visible extinction, thus an intrinsic weak $H\alpha$ emission.

Using either a tilted ring model or by matching the two sides of the galaxy with radially constant values of inclination and position angle, we found an inclination of 66° , a position angle of 150° , and a systemic velocity of 633 km s^{-1} , virtually identical to the values found by Begeman inside a radius of $180''$. The kinematical center was found to be centered on the bright nucleus. The final $H\alpha$ curve (Tab. 10 and Tab. A.5) is based on a Gaussian smoothed ($\sigma = 3''$) version of the velocity field.

Despite the very similar orientation parameters, the $H\alpha$ velocities stay up to 26 km s^{-1} below the beam smear-

ing corrected HI data in the inner part of the galaxy. Due to the low radio resolution ($>32''$) and the steepness of the rotation curve, it is conceivable that the first HI points have been over-corrected for beam smearing.

3.6. NGC 5985

This massive galaxy was observed with a wider filter (19\AA) but centered 3\AA bluer than the galaxy central wavelength. That, in conjunction with the high rotational velocity, prevented the reddest flux to reach the CCD. The velocity field is thus slightly incomplete on the receding side but a complete and reliable rotation curve can be derived using data away from the major axis. There is therefore no cut-off in rotation velocity but instead, an added uncertainty throughout the velocity plateau due to the lack of purely radially moving gas. The $H\alpha$ rotation curve was retrieved matching the two sides of the galaxy. The inclination and position angles were found to be respectively 58° and 15° .

For this galaxy an HI rotation curve has been derived from the WHISP^e data. The general procedures for the observations and reduction of the WHISP data are presented in Swaters et al. (2000), but details for this particular galaxy will be published in a future paper. The velocity field for NGC 5985 was derived by fitting Gaussians to the line profiles. Then, from a tilted-ring fit to the veloc-

^e www.astro.rug.nl/~whisp

ity field derived from the HI observations we found that the inclination varies little and ranges between 62° and 58° , and that the rotation angle is nearly constant at 15° . We therefore fixed the inclination at 60° and the position angle at 15° , very close to their H α counterparts.

Note that because of the lack of HI in the center, no HI rotation curve can be derived there. This shows the complementarity between H α and HI observations. Not only the former have higher resolution, thus reducing the problems associated with beam smearing, but also it may trace the rotation curve in regions where no HI has been detected.

4. Summary and Conclusions

It is well known that HI observations are commonly affected by beam smearing. The present data set is well suited to illustrate this fact. A useful test to estimate the reliability of HI observations is to compare the size of the radio beam width to the size of the galaxy. Bosma (1978) introduced the ratio $R_B \equiv R_H/S$ where R_H is the Holmberg radius and S is the radio beam major axis width. A more surface brightness independent ratio was introduced by van den Bosch et al. (2000): $R_{vdB} \equiv \alpha^{-1}/S$ where α^{-1} is the B-band stellar disk scale length. Table 3 compares those two ratios to the maximum difference between the H α and the HI on the rising part of the rotation curves.

NGC 5055, which shows the largest R_B and R_{vdB} , also has the largest ΔV_{max} . Looking at Fig. 8, the effect of beam smearing seems clearly visible in the inner 2 kpc. For the galaxy with the second largest R_B , NGC 2403, the beam smearing corrections of Begeman (1987) seem to work fine since there is a very good agreement ($\Delta V_{max} \leq 6.5 \text{ km s}^{-1}$) between the HI and the H α observations. However, for NGC 2841, it appears that the HI velocities were overcorrected for beam smearing by Begeman (1987). The results for those two galaxies show the difficulties related to beam smearing correction, and that high resolution data are still the best way to get the proper kinematics in the inner parts.

Not much can be said on the possible beam smearing effects for the 3 other galaxies since UGC 2259 has no H α in the center, NGC 5985 has no HI and NGC 6946 has a too high velocity dispersion which could be due to the presence of a bar. As was pointed out by Swaters (1999a), the magnitude of beam smearing does not only depends on the size of the beam, but also on details of the galaxy, such as its inclination, HI distribution and kinematics.

Amid the uncertainties that can affect rotation curves, non-circular motions like bars and local phenomena such as expanding bubbles or spiral arms can be a major source of error. Classical 1-D spectroscopy at any wavelength, while reaching a sufficient resolution, cannot easily deal with these problems. On the other hand, these phenomena can be efficiently tracked by the 2-D spectroscopic coverage from Fabry-Perot data (see also Schommer et al., 1993, for a similar conclusion in the context of distance in-

Table 3. Beam-to-galaxy size and beam smearing importance

Galaxy name	Beam width (S) "	R_B	R_{vdB} km s^{-1}	ΔV_{max}
UGC 2259	13.2	5.2	1.29	7.8
NGC 2403	26	26	4.62	6.5
NGC 6946	24.5	19	4.70	16.8
NGC 5055	12.8	46	8.51	23.9
NGC 2841 ^a	25	15	2.08	-34.0
NGC 5985	30	5.3	1	$\geq 10^b$

^a HI corrected for beam smearing

^b No HI data for the inner part

dicators). Depending on their orientation, bars can change the radial velocities in the inner parts of galaxies. Their signature may however be seen in the velocity field as a regular deviation from the typical projected circular velocities. None of the SB or SAB in our sample shows signs of these deviations though some of them have very low signal to noise in the center (UGC 2259 and NGC 5985) or very high velocity dispersion (NGC 6946). NGC 5055 shows strong activity inside 300 pc which can be interpreted either has an almost counter-rotating disk hosting a $9 \pm 2 \times 10^8 M_\odot$ object, or as a bipolar outflow. Gas kinematics alone tend to favor the bipolar outflow but peculiar stellar velocities in Afanasiev and Sil'chenko (2002) data would be more consistent with a rotating disk.

Complete 2-D velocity fields also allow independent determinations of inclination and position angles, kinematical centers and systemic velocities. This is a major gain over 1-D spectroscopy considering the sensitivity of the rotation curves to these parameters.

Acknowledgements. We warmly thank Jacques Boulesteix for his software and for fruitful discussions on Fabry-Perot data reduction, and the staff of the CFHT for their support during the Fabry-Perot data acquisition. We are indebted to Stéphanie Côté for the opportunity to re-observe NGC 5055 and to Olivier Hernandez who helped with the reduction of the NGC 2841 data. CC acknowledges grants from NSERC (Canada) and FQRNT (Québec).

References

- Afanasiev, V. L. and Sil'chenko, O. K., 2002, *A&A* 388, 461
 Amram, P., Balkowski, C., Boulesteix, J., Cayatte, V., Marcelin, M., and Sullivan, III, W., 1996, *A&A* 310, 737
 Amram, P., Boulesteix, J., Marcelin, M., Balkowski, C., Cayatte, V., and Sullivan, W., 1995, *A&AS* 113, 35
 Beauvais, C. and Bothun, G., 2001, *ApJSS* 136, 41
 Begeman, K., 1987, Ph.D. thesis, Rijksuniversiteit Groningen
 Blais-Ouellette, S., Amram, P., and Carignan, C., 2001, *AJ* 121, 1952, (Paper II)
 Blais-Ouellette, S., Carignan, C., Amram, P., and Côté, S., 1999, *AJ* 118, 2123, (Paper I)

- Bonnarel, F., Boulesteix, J., Georgelin, Y. P., Lecoarer, E., Marcelin, M., Bacon, R., and Monnet, G., 1988, *A&A* 189, 59
- Bosma, A., 1978, Ph.D. thesis, Rijksuniversiteit Groningen
- Carignan, C., Charbonneau, P., Boulanger, F., and Viallefond, F., 1990, *A&A* 234, 43
- Carignan, C., Sancisi, R., and Van Albada, T. S., 1988, *AJ* 95, 37
- Côté, S., Carignan, C., and Sancisi, R., 1991, *AJ* 102, 904
- de Blok, W. J. G., Bosma, A., and McGaugh, S., 2003, *MNRAS* 340, 657
- de Vaucouleurs, G. and Freeman, K. C., 1972, *Vistas in Astronomy* 14, 163
- Freedman, W. L., 1990, *ApJ* 355, L35
- Garrido, O., Marcelin, M., Amram, P., and Boulesteix, J., 2002, *A&A* 387, 821
- Gonzalez-Serrano, J. I. and Valentijn, E. A., 1991, *A&A* 242, 334
- Israel, F. P. and Baas, F., 2001, *A&A* 371, 433
- Kennicutt, R. C., 1988, *ApJ* 334, 144
- Macri, L. M., Stetson, P. B., Bothun, G. D., Freedman, W. L., Garnavich, P. M., Jha, S., Madore, B. F., and Richmond, M. W., 2001, *ApJ* 559, 243
- Moore, B., Ghigna, S., Governato, F., Lake, G., Quinn, T., Stadel, J., and Tozzi, P., 1999, *ApJ* 524, L19
- Moore, B., Governato, F., Quinn, T., Stadel, J., and Lake, G., 1998, *ApJ* 499, L5
- Navarro, J. F., Frenk, C. S., and White, S. D. M., 1996, *ApJ* 462, 563
- Navarro, J. F., Frenk, C. S., and White, S. D. M., 1997, *ApJ* 490, 493
- Navarro, J. F., Hayashi, E., Power, C., Jenkins, A., Frenk, C., White, S., Springel, V., Stadel, J., and Quinn, T., 2003, *The Inner Structure of LambdaCDM Halos III: Universality and Asymptotic Slopes*, astro-ph/0311231
- Pismis, P., Mampaso, A., Manteiga, M., Recillas, E., and Cruz Gonzalez, G., 1995, *AJ* 109, 140
- Roussel, H., Vigroux, L., Bosma, A., Sauvage, M., Bonoli, C., Gallais, P., Hawarden, T., Lequeux, J., Madden, S., and Mazzei, P., 2001, *A&A* 369, 473
- Schommer, R. A., Bothun, G. D., Williams, T. B., and Mould, J. R., 1993, *AJ* 105, 97
- Sharina, M. E., Karachentsev, I. D., and Tikhonov, N. A., 1997, *Pis ma Astronomicheskii Zhurnal* 23, 430
- Sofue, Y., 1996, *ApJ* 458, 120
- Sofue, Y., Tutui, Y., Honma, M., Tomita, A., Takamiya, T., Koda, J., and Takeda, Y., 1999, *ApJ* 523, 136
- Swaters, R., 1999a, in *ASP Conf. Ser. 182: Galaxy Dynamics - A Rutgers Symposium*, p. 369
- Swaters, R., 1999b, Ph.D. thesis, Rijksuniversiteit Groningen
- Swaters, R. A., Madore, B. F., and Trewhella, M., 2000, *ApJ* 531, L107
- Swaters, R. A., Madore, B. F., van den Bosch, F. C., and Balcells, M., 2003, *ApJ* 583, 732
- Thornley, M. D. and Mundy, L. G., 1997, *ApJ* 484, 202
- van den Bosch, F. C., Robertson, B. E., Dalcanton, J. J., and de Blok, W. J. G., 2000, *AJ* 119, 1579
- van der Kruit, P. C. and Bosma, A., 1978, *A&AS* 34, 259
- Weldrake, D. T. F., de Blok, W. J. G., and Walter, F., 2003, *MNRAS* 340, 12

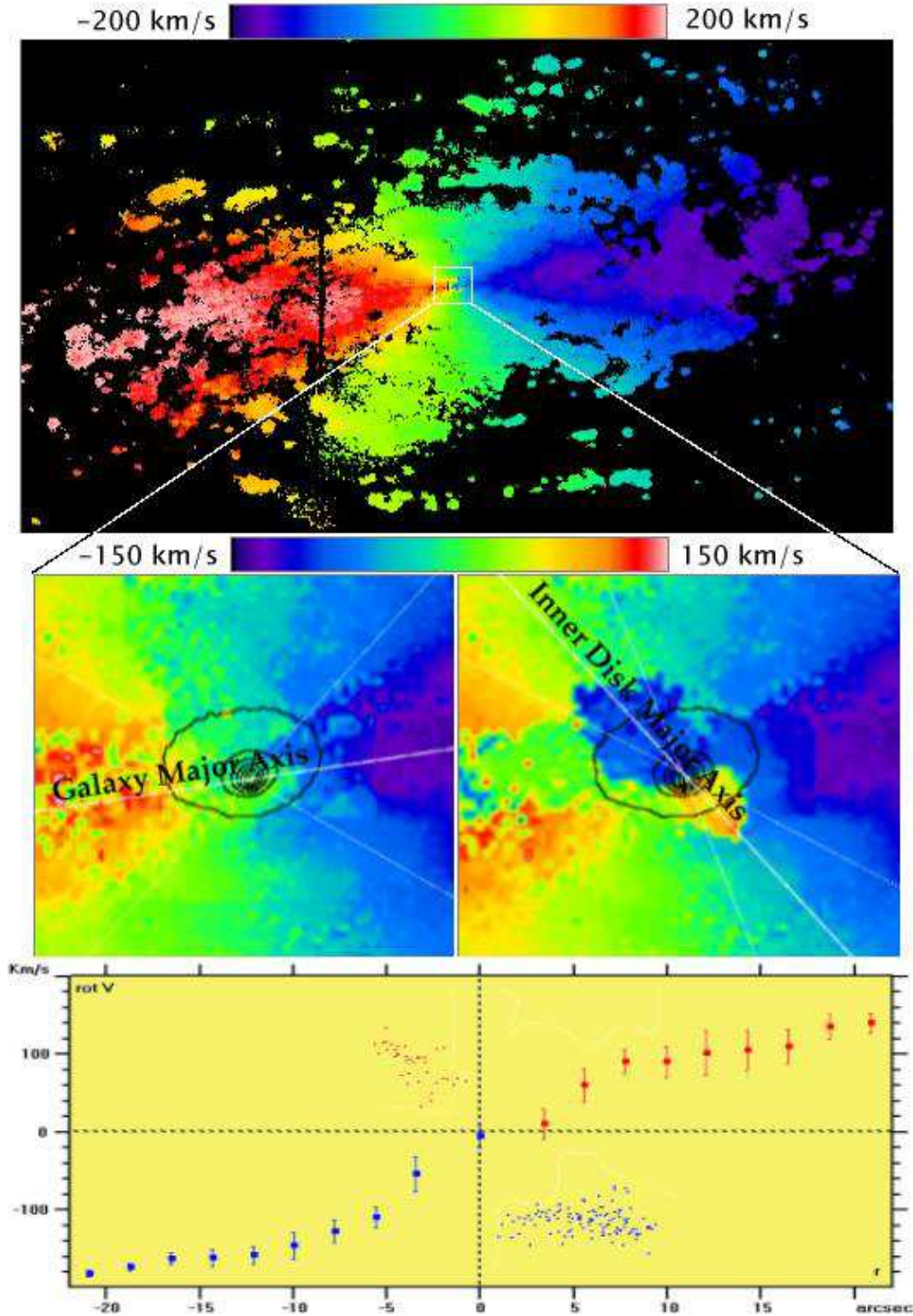


Fig. 9. *Top* Velocity field at full resolution for NGC 5055. *Middle* enlargements of the central regions for the two velocity components. *Bottom* velocity curve (4 pixels bins) for the main disk component and radial velocity minus systemic velocity (individual pixels) for the central outflow/disk.

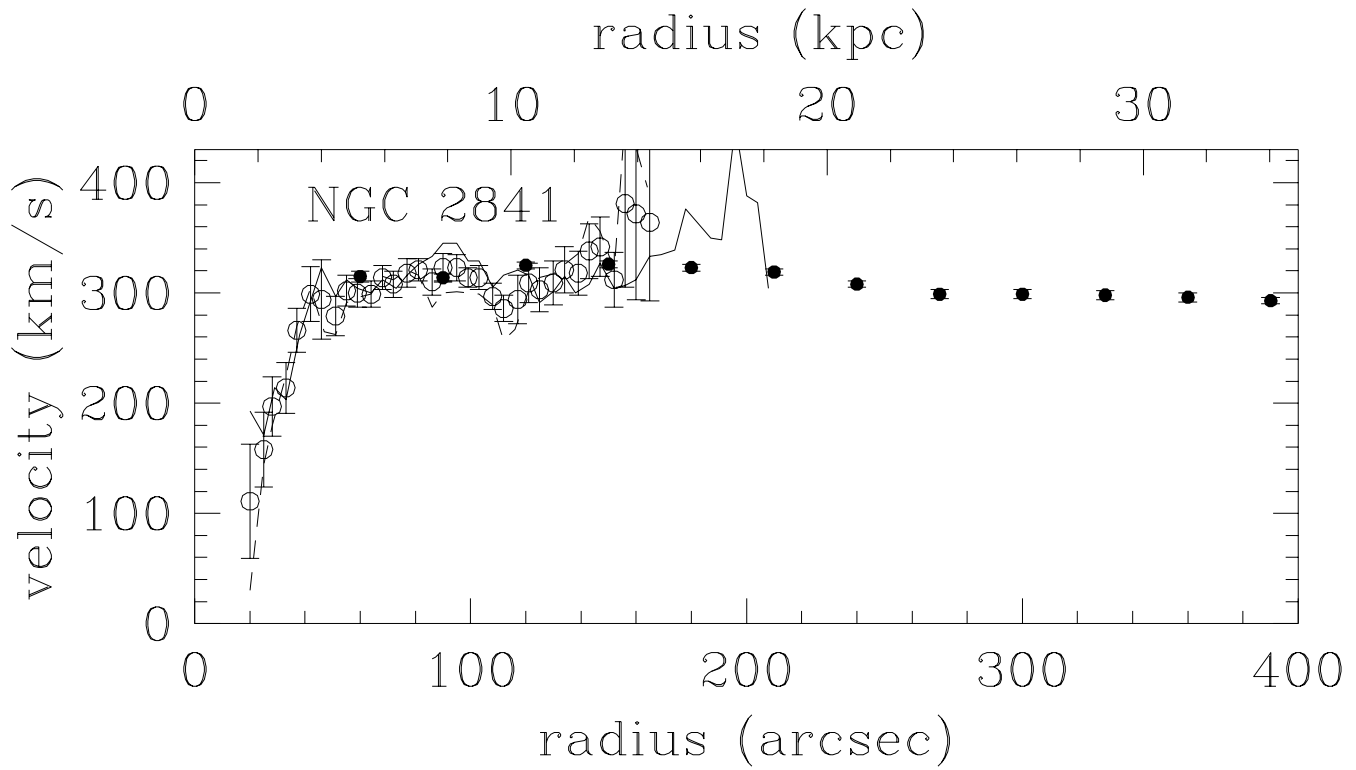


Fig. 10. H α rotation curve of NGC 2841 (open circles). Approaching and receding sides from H α data are indicated respectively by the dashed and continuous lines. The filled circles represent the beam smearing corrected HI rotation curve from Begeman (1987).

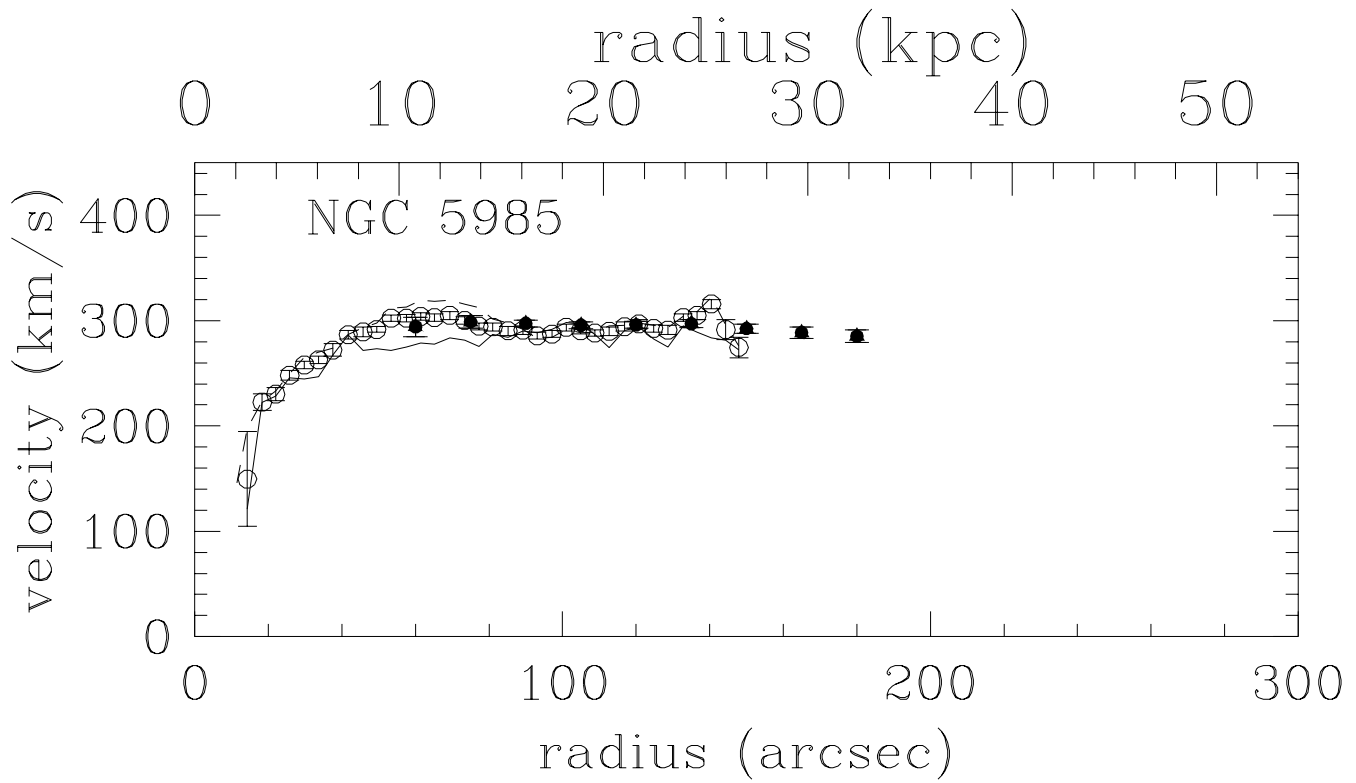


Fig. 11. H α rotation curve of NGC 5985 (open circles). Approaching and receding sides from H α data are indicated respectively by the dashed and continuous lines. The filled circles represent the HI rotation curve corrected for beam smearing.

Appendix A: Rotation Curves**Table A.1.** Optical rotation curve of UGC 2259 at 2.6'' resolution.

R arcsec	N_{app}	V_{app} km s^{-1}	σ_{ring} km s^{-1}	N_{rec}	V_{rec} km s^{-1}	σ_{ring} km s^{-1}	V km s^{-1}
1.4				5	0	28	0 ± 12
3.8				15	16	9	16 ± 2
6.4				17	28	13	28 ± 3
9.3				7	35	9	35 ± 3
11.6				15	45	15	45 ± 4
13.7				2	80	8	80 ± 5
17.4	14	55	5				55 ± 1
19.8	18	63	8				63 ± 2
22.8	16	64	10				64 ± 2
24.9	14	66	10				66 ± 3
28.0	41	68	12				68 ± 2
30.4	79	66	13				66 ± 1
33.2	80	74	14	6	73	10	74 ± 2
35.6	51	73	11	23	72	8	72 ± 2
38.4	57	78	12	53	72	6	75 ± 1
40.9	72	79	14	59	78	8	79 ± 1
43.6	92	80	13	74	80	9	80 ± 1
46.2	84	82	11	73	82	8	82 ± 1
48.9	65	83	9	51	87	5	85 ± 1
51.4	46	84	14	38	84	8	84 ± 2
54.0	45	86	14	24	79	10	84 ± 2
56.7	35	85	10	12	76	9	83 ± 2
59.4	25	74	12	13	68	6	72 ± 2
61.9	19	71	8	38	69	5	69 ± 1
64.3	7	75	5	41	69	6	70 ± 1
67.3				28	75	15	75 ± 3
69.4				15	76	16	76 ± 4

Table A.2. Optical rotation curve of NGC 2403 at 6.6'' resolution.

R arcsec	N_{app}	V_{app} km s^{-1}	σ_{ring} km s^{-1}	N_{rec}	V_{rec} km s^{-1}	σ_{ring} km s^{-1}	V km s^{-1}
10.3	49	29	13	48	21	9	25 ± 2
16.7	79	41	14	79	32	11	36 ± 1
23.2	116	45	15	116	43	15	44 ± 1
29.96	148	55	16	148	52	14	53 ± 1
36.4	178	67	18	179	56	15	62 ± 1
43.0	209	68	22	209	65	15	67 ± 1
49.6	251	75	23	251	72	16	73 ± 1
56.2	274	78	23	274	73	19	76 ± 1
62.8	312	77	21	312	76	20	76 ± 1
69.4	342	79	19	342	77	18	78 ± 1
76.0	361	83	17	375	78	14	80 ± 1
83.0	379	88	20	408	82	15	85 ± 1
89.1	425	91	19	441	86	15	88 ± 1
95.7	451	91	21	471	87	15	89 ± 1
102.3	479	94	15	506	90	18	92 ± 1
108.9	538	98	21	540	93	19	95 ± 1
115.5	576	97	21	574	93	19	95 ± 1
122.1	600	98	22	583	95	21	97 ± 1
128.7	629	102	19	598	97	22	99 ± 1
135.4	659	104	20	627	97	22	101 ± 1
141.9	695	103	19	651	96	19	100 ± 1
148.5	728	102	20	634	97	18	100 ± 1
155.1	762	100	20	610	100	16	100 ± 1
161.8	788	98	21	667	100	18	99 ± 1
168.3	806	98	20	711	102	19	100 ± 1
174.9	852	99	21	766	101	19	100 ± 1
181.5	870	98	20	779	103	18	100 ± 1
188.1	926	97	23	753	107	19	101 ± 1
194.7	918	98	23	690	108	22	102 ± 1
201.3	948	99	28	698	111	22	104 ± 1
207.9	949	98	30	661	111	20	103 ± 1
214.5	1010	98	30	656	111	20	103 ± 1
221.1	1069	101	28	644	112	22	105 ± 1
227.6	1084	106	23	600	115	21	109 ± 1
234.3	1076	109	24	510	118	22	112 ± 1
240.9	1150	111	23	462	124	21	114 ± 1
247.4	1204	112	26	321	132	25	116 ± 1
254.0	1133	116	28	304	136	21	120 ± 1
260.7	1089	116	30	291	135	20	120 ± 1
267.2	1058	115	30	236	128	20	118 ± 1
273.9	1127	114	31	163	127	24	115 ± 1
280.6	1130	112	30	158	127	23	114 ± 1
287.1	1032	110	27	202	118	21	112 ± 1
293.6	1009	107	24	182	114	18	108 ± 1
300.1	1085	110	23	208	118	18	111 ± 1
306.9	1043	113	24	264	121	15	115 ± 1
313.4	935	115	25	240	119	16	115 ± 1
320.1	1015	118	26	269	118	16	118 ± 1
326.7	1068	118	24	202	117	12	118 ± 1
333.3	1076	121	23	232	121	14	121 ± 1
339.8	833	122	25	201	124	12	123 ± 1
346.5	776	121	25	176	123	12	122 ± 1

Table A.2 *continued*

R arcsec	N_{app}	V_{app} km s^{-1}	σ_{ring} km s^{-1}	N_{rec}	V_{rec} km s^{-1}	σ_{ring} km s^{-1}	V km s^{-1}
353.1	853	120	24	159	124	18	120 ± 1
359.7	834	119	20	160	127	11	120 ± 1
366.3	789	119	23	148	128	11	121 ± 1
372.9	691	122	25	141	129	29	123 ± 1
379.5	640	120	25	116	141	10	123 ± 1
386.1	748	119	22	105	149	7	123 ± 1
392.9	725	118	23	142	153	13	124 ± 1
399.4	759	120	21	172	151	12	125 ± 1
405.6	620	122	29	166	145	17	126 ± 1
412.5	492	123	32	127	145	33	128 ± 2
418.9	485	125	29	106	143	33	128 ± 2
425.3	453	128	28	39	156	29	130 ± 2
433.1	307	128	26	11	115	3	127 ± 1
438.8	270	125	40	23	113	5	124 ± 2
443.9	281	118	45	2	109	0	118 ± 3
452.6	310	121	42	31	129	4	122 ± 2
458.5	318	128	29	40	131	4	129 ± 2
462.9				5	133	9	133 ± 4
465.3	304	134	29				134 ± 2
471.8	278	142	30				142 ± 2
478.3	220	147	33				147 ± 2
484.4	107	145	32				145 ± 3
490.2	15	114	16				114 ± 4
500.3	3	116	15				116 ± 9
505.9	66	133	35				133 ± 4
511.5	139	124	34				124 ± 3
518.2	170	128	29				128 ± 2
524.7	173	130	33				130 ± 2
531.2	148	126	34				126 ± 3
537.6	91	118	19				118 ± 2
544.7	96	125	19				125 ± 2
551.1	128	127	22				127 ± 2
557.8	152	134	25				135 ± 2
564.4	144	129	27				129 ± 2
570.7	130	135	28				135 ± 2
576.8	72	125	26				125 ± 3
583.9	18	117	21				117 ± 5
589.9	7	114	21				114 ± 8

Table A.3. Optical rotation curve of NGC 6946 at 4.4'' resolution.

R arcsec	N_{app}	V_{app} km s^{-1}	σ_{ring} km s^{-1}	N_{rec}	V_{rec} km s^{-1}	σ_{ring} km s^{-1}	V km s^{-1}
6.9	70	103	28	66	110	71	107 ± 7
11.2	109	124	27	105	150	22	136 ± 2
15.4	156	141	27	113	126	34	135 ± 3
19.7	201	150	30	88	115	47	140 ± 3
24.4	243	139	33	76	85	56	126 ± 4
28.7	247	134	31	119	104	28	124 ± 2
33.0	184	128	39	151	131	41	129 ± 3
37.1	150	108	27	118	134	53	120 ± 4
41.9	155	96	33	71	146	52	112 ± 4
46.4	217	109	44	78	113	48	110 ± 4
50.8	292	108	46	96	97	62	106 ± 4
55.1	390	113	45	221	116	39	114 ± 2
59.5	428	120	38	301	117	28	119 ± 2
63.8	420	118	35	423	131	26	125 ± 1
68.3	449	118	38	421	138	20	128 ± 1
72.6	529	118	24	425	140	19	128 ± 1
77.0	626	117	25	419	144	19	128 ± 1
81.5	707	114	22	579	143	20	127 ± 1
85.8	682	111	23	615	138	22	124 ± 1
90.2	682	111	21	668	139	24	125 ± 1
94.6	652	113	26	674	137	21	125 ± 1
99.0	723	113	29	703	135	19	124 ± 1
103.4	635	111	26	553	135	22	122 ± 1
107.8	609	120	20	522	135	23	127 ± 1
112.2	598	128	18	561	134	22	131 ± 1
116.6	703	134	17	552	136	20	135 ± 1
121.0	661	139	18	649	142	17	141 ± 1
125.5	661	139	20	800	145	16	142 ± 1
129.8	700	143	20	925	148	19	146 ± 1
134.2	680	146	26	1016	150	29	149 ± 1
138.6	675	137	22	1052	150	24	145 ± 1
143.0	713	143	18	1068	148	23	146 ± 1
147.4	668	147	17	1031	155	21	152 ± 1
151.8	661	152	15	924	157	32	155 ± 1
156.2	782	153	15	719	159	38	156 ± 1
160.7	807	155	14	706	162	36	158 ± 1
165.0	830	156	17	689	161	38	158 ± 1
169.4	863	155	18	684	156	35	155 ± 1
173.8	837	162	16	553	156	37	159 ± 1
178.1	706	164	18	495	160	42	162 ± 1
182.6	533	166	19	399	155	37	161 ± 1
187.0	408	171	21	430	154	30	162 ± 1
191.4	382	174	19	420	158	29	165 ± 1
195.8	396	176	17	309	161	26	169 ± 1
200.2	317	169	15	329	160	35	165 ± 2
204.7	235	171	14	342	164	23	167 ± 1
209.1	295	172	17	346	165	32	168 ± 1
213.4	312	175	16	429	172	20	174 ± 1
217.8	250	174	14	332	175	23	175 ± 1
222.2	193	172	13	504	163	38	165 ± 2
226.7	227	169	16	380	161	23	164 ± 1
231.2	272	180	20	411	160	27	168 ± 1

Table A.3 *continued*

R arcsec	N_{app}	V_{app} km s^{-1}	σ_{ring} km s^{-1}	N_{rec}	V_{rec} km s^{-1}	σ_{ring} km s^{-1}	V km s^{-1}
235.3	286	187	24	607	154	35	165 ± 1
239.9	344	188	27	471	156	26	169 ± 1
244.2	497	182	26	443	167	24	175 ± 1
248.6	572	177	34	542	163	24	170 ± 1
253.0	409	175	35	628	163	24	168 ± 1
257.4	270	178	32	743	168	24	170 ± 1
262.0	140	188	30	816	169	26	172 ± 1
266.2	154	206	44	797	163	31	170 ± 2
270.2	57	208	46	745	162	28	165 ± 2
274.8	19	238	15	675	158	30	160 ± 1
279.3				563	159	29	159 ± 1
283.7				469	162	30	162 ± 1
288.2				380	178	28	178 ± 1
292.4				283	183	30	183 ± 2
296.7				162	175	31	175 ± 2
300.9				48	154	26	154 ± 26

Table A.4. Optical rotation curve of NGC 5055 at 2.2'' resolution.

R arcsec	N_{app}	V_{app} km s^{-1}	σ_{ring} km s^{-1}	N_{rec}	V_{rec} km s^{-1}	σ_{ring} km s^{-1}	V km s^{-1}
3	36	64	55	36	3	36	34 ± 11
6	59	111	25	59	64	33	88 ± 5
8	85	130	31	85	86	38	108 ± 5
10	108	147	33	108	89	42	118 ± 5
12	131	170	21	124	143	21	156 ± 3
14	153	169	17	129	142	22	155 ± 2
17	182	174	11	172	148	21	161 ± 2
19	201	179	9	201	150	21	164 ± 2
21	228	184	13	228	149	15	167 ± 1
23	254	186	19	254	153	14	169 ± 1
25	277	184	19	275	156	14	170 ± 1
28	291	183	16	291	159	17	171 ± 1
30	323	185	15	315	164	18	175 ± 1
32	347	186	13	339	170	16	178 ± 1
34	373	185	15	373	173	17	179 ± 1
36	387	185	16	384	177	13	181 ± 1
39	423	188	14	423	178	10	183 ± 1
41	443	191	12	443	180	10	185 ± 1
43	462	192	11	460	180	11	186 ± 1
45	487	193	11	486	180	11	187 ± 1
47	514	196	11	512	182	10	189 ± 1
50	544	198	11	512	185	10	191 ± 1
52	558	199	11	512	192	10	195 ± 1
54	573	199	10	515	198	13	198 ± 1
56	606	200	11	506	200	12	200 ± 1
58	631	201	10	560	202	15	201 ± 1
61	654	202	10	602	203	15	203 ± 1
63	686	202	9	604	208	13	205 ± 1
65	695	201	10	641	209	12	205 ± 1
67	706	202	10	678	209	18	206 ± 1
69	718	201	11	647	209	16	205 ± 1
72	725	200	12	535	207	18	204 ± 1
74	742	197	16	520	208	15	203 ± 1
76	778	195	19	573	207	17	201 ± 1
78	782	195	22	611	205	18	200 ± 1
80	825	195	20	677	202	19	199 ± 1
83	841	196	18	686	201	20	199 ± 1
85	863	195	16	714	198	22	197 ± 1
87	883	195	15	642	198	21	197 ± 1
89	833	196	16	617	194	27	195 ± 1
91	826	197	15	600	195	24	196 ± 1
93	864	197	15	665	191	26	194 ± 1
96	893	197	14	724	188	30	192 ± 1
98	910	197	14	631	191	28	194 ± 1
100	931	198	15	678	189	28	193 ± 1
102	935	200	16	792	193	23	196 ± 1
104	902	202	15	885	197	21	199 ± 1
107	870	204	14	977	195	27	199 ± 1
109	928	204	13	955	196	25	200 ± 1
111	935	204	14	896	198	25	201 ± 1
113	1013	203	15	851	200	25	201 ± 1
116	976	204	14	814	199	29	202 ± 1

Table A.4 *continued*

R arcsec	N_{app}	V_{app} km s^{-1}	σ_{ring} km s^{-1}	N_{rec}	V_{rec} km s^{-1}	σ_{ring} km s^{-1}	V km s^{-1}
118	987	205	13	799	199	33	202 ± 1
120	1046	205	12	778	202	30	203 ± 1
122	1100	205	13	771	204	31	204 ± 1
124	1219	204	12	802	203	34	203 ± 1
127	1268	204	12	839	203	34	204 ± 1
129	1282	205	11	913	203	34	204 ± 1
131	1323	207	11	957	208	29	207 ± 1
133	1259	209	12	918	209	27	209 ± 1
135	1214	209	12	810	208	29	209 ± 1
137	1160	210	12	741	209	26	210 ± 1
140	1111	208	12	623	209	27	209 ± 1
142	1116	208	12	602	209	30	209 ± 1
144	1093	207	12	649	207	33	207 ± 1
146	1132	206	12	624	207	34	206 ± 1
149	1153	205	13	605	210	28	208 ± 1
151	1175	204	13	619	211	22	208 ± 1
153	1175	204	15	622	209	24	207 ± 1
155	1230	205	16	587	206	28	206 ± 1
157	1177	206	17	530	206	30	206 ± 1
160	1080	208	16	458	203	34	205 ± 2
162	980	208	13	467	200	32	204 ± 2
164	988	209	11	537	204	26	206 ± 1
166	1022	211	12	711	205	22	208 ± 1
168	990	211	12	630	203	22	207 ± 1
171	1032	212	13	588	201	22	206 ± 1
173	1077	209	14	606	200	24	205 ± 1
175	1009	209	12	570	203	28	206 ± 1
177	1050	208	11	542	206	21	207 ± 1
179	1018	207	11	507	207	21	207 ± 1
182	1004	208	13	529	207	20	207 ± 1
184	960	208	13	593	203	24	206 ± 1
186	836	209	14	688	202	27	205 ± 1
188	674	210	14	591	200	30	205 ± 1
190	608	212	12	569	199	29	206 ± 1
192	499	213	11	539	201	28	207 ± 1
195	472	213	11	623	204	26	208 ± 1
197	415	211	11	714	204	26	207 ± 1
199	296	208	14	702	207	25	208 ± 1
201	276	202	27	599	207	26	205 ± 2
204	321	198	35	619	210	28	204 ± 2
206	389	202	19	603	217	17	209 ± 1
208	341	200	13	575	217	13	208 ± 1
210	327	199	11	436	215	15	207 ± 1
212	276	201	17	309	216	17	209 ± 1
214	193	202	14	283	214	20	208 ± 2
217	112	199	15	283	208	29	203 ± 2
219	82	192	28	278	208	27	200 ± 3
221	67	196	15	252	206	27	201 ± 2
223	56	208	10	293	213	22	210 ± 2
226	20	218	19	344	213	19	215 ± 4
227	10	223	28	376	211	19	217 ± 9
233	13	190	23	267	208	14	199 ± 6
234	21	167	17	275	211	19	189 ± 4
237	29	181	45	282	217	27	199 ± 8
239	21	174	78	209	217	37	195 ± 17
241	42	180	20	218	212	33	196 ± 4

Table A.4 *continued*

R arcsec	N_{app}	V_{app} km s^{-1}	σ_{ring} km s^{-1}	N_{rec}	V_{rec} km s^{-1}	σ_{ring} km s^{-1}	V km s^{-1}
243	29	191	13	138	219	29	205 ± 3
245	51	192	5	69	221	34	206 ± 4
247	28	192	7	65	235	52	213 ± 7
251	1	214	0	96	234	20	224 ± 2
255	8	204	4	86	237	11	221 ± 2
256	23	208	17	119	245	11	227 ± 4
259	43	199	31	165	238	14	219 ± 5
261	49	208	14	111	238	15	223 ± 2
263	73	205	17	44	233	21	219 ± 4
265	78	206	18	33	249	34	227 ± 6
267	81	204	30	9	218	92	211 ± 31
270	110	207	21	6	241	15	224 ± 6
272	133	206	22	16	234	15	220 ± 4
274	126	200	28	28	231	20	215 ± 4
276	94	205	21	26	223	14	214 ± 3
278	92	212	17	21	230	10	221 ± 3
281	120	217	21	2	139	19	178 ± 14
283	134	205	25	3	47	4	126 ± 3
285	128	201	28	1	29	0	115 ± 2
287	144	196	31	4	195	51	195 ± 25
289	146	198	30	12	112	53	155 ± 15
291	112	199	23	7	117	16	158 ± 7
294	66	199	23				199 ± 3
296	56	182	24				182 ± 3
298	86	176	18				176 ± 2
300	93	177	19				177 ± 2
303	101	172	23				172 ± 2
305	118	164	35				164 ± 3
307	76	160	14				160 ± 2

Table A.5. Optical rotation curve of NGC 2841 at 4.4'' resolution.

R arcsec	N_{app}	V_{app} km s^{-1}	σ_{ring} km s^{-1}	N_{rec}	V_{rec} km s^{-1}	σ_{ring} km s^{-1}	V km s^{-1}
20	41	193	160	26	30	232	111 ± 52
25	19	171	103	42	144	155	158 ± 34
28	21	214	90	46	180	126	197 ± 27
33	54	203	80	43	225	133	214 ± 23
37	47	262	112	33	270	62	266 ± 20
42	58	293	155	30	304	75	299 ± 25
46	60	323	177	63	265	225	294 ± 36
51	113	297	161	128	262	117	279 ± 18
55	151	312	154	231	291	90	302 ± 14
59	171	304	150	276	296	107	300 ± 13
64	176	300	142	282	299	89	299 ± 12
68	237	312	152	227	315	78	314 ± 11
72	265	304	159	209	312	98	308 ± 12
77	286	316	153	167	321	113	318 ± 13
81	344	326	145	130	316	68	321 ± 10
86	314	333	147	138	287	94	310 ± 12
90	306	345	159	197	300	129	323 ± 13
95	311	345	185	240	301	104	323 ± 12
99	339	329	147	262	300	68	314 ± 9
103	352	329	122	226	299	127	314 ± 11
108	399	305	147	227	289	146	297 ± 12
112	348	316	127	196	257	139	286 ± 12
117	391	321	139	120	267	232	294 ± 22
121	365	316	129	98	302	167	309 ± 18
125	319	291	154	105	314	185	303 ± 20
130	349	301	152	124	317	208	309 ± 20
134	376	315	155	124	326	211	321 ± 21
139	284	300	155	112	336	192	318 ± 20
143	185	308	173	104	369	222	338 ± 25
147	129	327	205	87	356	183	342 ± 27
152	99	304	159	59	321	145	312 ± 25
156	116	307	174	19	455	324	381 ± 76
160	116	312	191	8	432	214	372 ± 78
165	84	333	176	7	396	180	364 ± 71
169	76	335	176				335 ± 20
174	48	339	206				339 ± 30
178	22	376	194				376 ± 41
187	17	350	254				350 ± 62
191	21	348	221				348 ± 48
196	16	453	226				453 ± 56
200	20	388	207				388 ± 46
204	15	382	131				382 ± 34
208	3	304	82				304 ± 48

Table A.6. Optical rotation curve of NGC 5985 at 4'' resolution.

R arcsec	N_{app}	V_{app} km s^{-1}	σ_{ring} km s^{-1}	N_{rec}	V_{rec} km s^{-1}	σ_{ring} km s^{-1}	V km s^{-1}
11.5	1	146	-				146 \pm -
14.3	6	197	20	10	121	179	150 \pm 45
18.4	11	223	34	32	222	37	223 \pm 8
22.0	29	233	44	43	228	27	230 \pm 6
25.8	73	250	38	43	246	31	248 \pm 5
29.8	82	265	28	44	244	29	258 \pm 4
33.6	89	270	17	38	247	36	263 \pm 4
37.5	89	274	24	33	267	60	272 \pm 6
41.7	105	287	22	36	286	42	287 \pm 4
45.7	125	293	16	29	272	57	289 \pm 5
49.4	134	298	27	45	273	25	292 \pm 3
53.4	147	312	31	45	272	25	302 \pm 3
57.6	155	313	49	60	275	24	302 \pm 4
61.4	169	319	50	104	279	29	304 \pm 3
65.2	141	318	33	88	278	38	303 \pm 3
69.3	130	320	32	89	283	46	305 \pm 4
73.4	112	315	30	93	282	40	300 \pm 3
77.3	125	313	39	117	276	31	295 \pm 3
81.1	108	301	45	109	287	28	294 \pm 4
85.2	82	298	50	103	284	33	290 \pm 4
89.2	86	292	45	113	290	35	291 \pm 4
93.1	102	283	37	116	288	31	286 \pm 3
97.1	141	284	34	92	292	37	287 \pm 3
101.0	169	292	27	63	298	39	294 \pm 3
105.0	160	288	29	55	297	34	290 \pm 3
108.8	153	289	33	64	287	30	288 \pm 3
112.7	124	295	30	45	275	43	290 \pm 4
116.9	128	296	29	36	291	46	294 \pm 4
120.7	108	298	22	26	294	43	297 \pm 4
124.8	91	296	22	29	283	33	293 \pm 4
128.6	93	294	36	14	275	25	291 \pm 4
132.8	93	304	18	19	295	31	303 \pm 3
136.6	85	309	24	20	289	30	305 \pm 4
140.5	76	322	37	15	284	18	316 \pm 4
144.4	21	296	52	10	282	13	291 \pm 10
147.9	9	276	36	6	272	10	275 \pm 10
76.3	18	290	43				290 \pm 10
78.2	21	314	14				314 \pm 3
79.9	17	296	64				296 \pm 16
82.2	30	310	13				310 \pm 2
164.4	19	303	17				303 \pm 4
168.0	4	275	10				275 \pm 5

Table A.7. HI rotation curve of NGC 5985 at $\sim 10''$ binning ($30''$ resolution).

R arcsec	V km s^{-1}
60	294.2 ± 9.21
75	299.0 ± 5.94
90	297.3 ± 3.31
105	295.6 ± 3.42
120	295.9 ± 3.23
135	297.1 ± 3.72
150	292.4 ± 4.49
165	288.6 ± 5.40
180	285.1 ± 5.89